INTERNATIONAL JOURNAL FOR NUMERICAL METHODS IN FLUIDS
Int. J. Numer. Meth. Fluids 2006; **50**:767–793
Published online 15 September 2005 in Wiley InterScience (www.interscience.wiley.com). DOI: 10.1002/fld.1065

Implicit application of non-reflective boundary conditions for Navier–Stokes equations in generalized coordinates

Xiangying Chen*,†,§ and Ge-Cheng Zha‡,¶

Department of Mechanical and Aerospace Engineering, University of Miami, Coral Gables, FL 33124, U.S.A.

SUMMARY

The non-reflective boundary conditions (NRBC) for Navier–Stokes equations originally suggested by Poinsot and Lele (*J. Comput. Phys.* 1992; **101**:104–129) in Cartesian coordinates are extended to generalized coordinates. The characteristic form Navier–Stokes equations in conservative variables are given. In this characteristic-based method, the NRBC is implicitly coupled with the Navier–Stokes flow solver and are solved simultaneously with the flow solver. The calculations are conducted for a subsonic vortex propagating flow and the steady and unsteady transonic inlet-diffuser flows. The results indicate that the present method is accurate and robust, and the NRBC are essential for unsteady flow calculations. Copyright © 2005 John Wiley & Sons, Ltd.

KEY WORDS: non-reflective boundary conditions; Navier–Stokes equations; generalized coordinates

1. INTRODUCTION

The accuracy of unsteady flow calculations relies on accurate treatment of boundary conditions. Due to the limitation of computer resources, usually only a finite computational domain is considered for a flow calculation. This means that we have to 'cut off' the domain that is not of our primary interest. However, the cut boundaries may cause artificial wave reflections, which may include both physical waves and numerical waves [1]. Such waves may bounce back and forth within the computational domain and may seriously contaminate the solutions and produce misleading results. This is particularly true for internal flows such as the flows in turbomachinery, in which the computational domain usually is confined very near the solid

*Correspondence to: Xiangying Chen, Department of Mechanical and Aerospace Engineering, University of Miami, Coral Gables, FL 33124, U.S.A.
†E-mail: xychen@apollo.eng.miami.edu, shawn_xy_2000@yahoo.com
‡E-mail: zha@apollo.eng.miami.edu
§Post Doctoral Associate.
¶Associate Professor.

Contract/grant sponsor: AFOSR; contract/grant number: F49620-03-1-0253

Received 5 January 2005
Revised 8 July 2005
Accepted 11 July 2005

objects. For example, previous studies indicated that the different treatments of numerical perturbation at upstream and downstream boundaries can change the compressor blade stall inception pattern [2, 3].

The currently often used non-reflective boundary conditions (NRBC) for unsteady internal flows are based on eigenvalue analysis of linearized Euler equations developed by Giles [4]. However, Giles' method may only apply to the inviscid solutions which require the far-field flow to be uniform so that the propagation waves have the Fourier mode shapes. For viscous flows, the mean flow in the downstream far-field region may be non-uniform due to the airfoil or blade wakes, which means that there will be no Fourier mode shapes. In addition, the inconsistency of the Navier–Stokes governing equations for the inner domain and linearized Euler equations at far-field boundary may also cause numerical wave reflections.

The more rigorous treatment of NRBC for Navier–Stokes equations is the one suggested by Poinsot and Lele in 1992 [1] for direct numerical simulation of turbulence. However, the NRBC given by Poinsot and Lele [1] is only for the regular mesh aliened with the coordinate axises in Cartesian coordinates. The explicit time marching scheme was used in the calculation of Poinsot and Lele. For practical engineering applications, the body fitted generalized coordinates are usually necessary. In 2000, Kim and Lee [5] made an effort to extend the NRBC of Poinsot and Lele from the Cartesian coordinates to generalized coordinates. However, in their derivation, a flaw was made by absorbing the eigenvector matrix into the partial derivatives, their formulations apply only if: (1) it is 1-D equation; (2) the eigenvector matrix is constant in the flow field; and (3) the partial differential equations satisfy Pfaff's condition. For multi-dimensional Navier–Stokes equations, all these three conditions are not satisfied [6, 7]. Hence, the wave amplitude vector derived in Reference [5] is erroneous.

More recently, based on the characteristic approach of Poinsot and Lele [1], Bruneau and Creuse [8] suggested a variation of the approximate treatment of the incoming wave amplitude in the exit boundary conditions by assuming that the pressure and velocity values will 'convect' with time to the location where the phantom cells are located. The results show the method works well. Prosser and Schluter [9] used an approach based on a low Mach number asymptotic expansion of the governing equations to improve the specification of time-dependent boundary conditions. With the help of the local one-dimensional inviscid (LODI) relations, Moureau *et al.* [10] implemented characteristic boundary conditions for multi-component mixtures in DNS and LES computations using a modified NRBC formulation.

The purpose of this paper is to extend the NRBC system from Cartesian coordinates to generalized coordinates and apply it numerically for unsteady calculations in an implicit time marching method. The NRBC system used in this paper is based on the equations given by Poinsot and Lele [1] in Cartesian coordinates, which is the foundation of other NRBC methods including those of Bruneau and Creuse [8] and Prosser and Schluter [9]. In a finite difference or finite volume approach, the governing equations are more straightforward to be solved in generalized coordinates, in which a complex physical domain becomes a rectangular computational domain (for 2-D case) or a hexahedral computational domain (for 3-D case) with equal grid spacings. The moving grid effect can be naturally included in the generalized coordinates. Strictly speaking, for finite differencing or finite volume methods, only solving the equations in generalized coordinates can preserve the accuracy of high-order numerical schemes.

In general, implicit methods permit a larger time step and are widely used for many practical applications. To be consistent with the implicit solver of the inner domain, in this

paper, the NRBC equations are implicitly discretized and solved simultaneously in a fully coupled manner. Two numerical cases are tested in this paper: a vortex propagating through a outflow boundary and a transonic inlet-diffuser flow with shock–boundary layer interaction. The numerical results indicate that the present methodology is robust and accurate.

2. GOVERNING EQUATIONS

The 3-D compressible Reynolds–averaged Navier–Stokes equations (RANS) with Favre mass average are solved for the flow field in generalized coordinates, which can be expressed as

$$\frac{\partial \mathbf{Q}'}{\partial t}+\frac{\partial \mathbf{E}'}{\partial \xi}+\frac{\partial \mathbf{F}'}{\partial \eta}+\frac{\partial \mathbf{G}'}{\partial \zeta}=\frac{1}{Re}\left(\frac{\partial \mathbf{E}'_v}{\partial \xi}+\frac{\partial \mathbf{F}'_v}{\partial \eta}+\frac{\partial \mathbf{G}'_v}{\partial \zeta}\right) \tag{1}$$

where Re is the Reynolds number and

$$\mathbf{Q}'=\frac{\mathbf{Q}}{J} \tag{2}$$

$$\mathbf{E}'=\frac{1}{J}(\xi_x\mathbf{E}+\xi_y\mathbf{F}+\xi_z\mathbf{G}) \tag{3}$$

$$\mathbf{F}'=\frac{1}{J}(\eta_x\mathbf{E}+\eta_y\mathbf{F}+\eta_z\mathbf{G}) \tag{4}$$

$$\mathbf{G}'=\frac{1}{J}(\zeta_x\mathbf{E}+\zeta_y\mathbf{F}+\zeta_z\mathbf{G}) \tag{5}$$

$$\mathbf{E}'_v=\frac{1}{J}(\xi_x\mathbf{E}_v+\xi_y\mathbf{F}_v+\xi_z\mathbf{G}_v) \tag{6}$$

$$\mathbf{F}'_v=\frac{1}{J}(\eta_x\mathbf{E}_v+\eta_y\mathbf{F}_v+\eta_z\mathbf{G}_v) \tag{7}$$

$$\mathbf{G}'_v=\frac{1}{J}(\zeta_x\mathbf{E}_v+\zeta_y\mathbf{F}_v+\zeta_z\mathbf{G}_v) \tag{8}$$

where the variable vector $\mathbf{Q}$, and inviscid flux vectors $\mathbf{E}$, $\mathbf{F}$, and $\mathbf{G}$ are

$$\mathbf{Q}=\begin{pmatrix}\bar{\rho}\\ \bar{\rho}\tilde{u}\\ \bar{\rho}\tilde{v}\\ \bar{\rho}\tilde{w}\\ \bar{\rho}\tilde{e}\end{pmatrix},\quad \mathbf{E}=\begin{pmatrix}\bar{\rho}\tilde{u}\\ \bar{\rho}\tilde{u}\tilde{u}+\tilde{p}\\ \bar{\rho}\tilde{u}\tilde{v}\\ \bar{\rho}\tilde{u}\tilde{w}\\ (\bar{\rho}\tilde{e}+\tilde{p})\tilde{u}\end{pmatrix}$$

$$\mathbf{F}=\begin{pmatrix}\bar{\rho}\tilde{v}\\ \bar{\rho}\tilde{u}\tilde{v}\\ \bar{\rho}\tilde{v}\tilde{v}+\tilde{p}\\ \bar{\rho}\tilde{w}\tilde{v}\\ (\bar{\rho}\tilde{e}+\tilde{p})\tilde{v}\end{pmatrix},\quad \mathbf{G}=\begin{pmatrix}\bar{\rho}w\\ \bar{\rho}\tilde{u}\tilde{w}\\ \bar{\rho}\tilde{v}\tilde{w}\\ \bar{\rho}\tilde{w}\tilde{w}+\tilde{p}\\ (\bar{\rho}\tilde{e}+\tilde{p})\tilde{w}\end{pmatrix}$$

and the viscous flux vectors are given by

$$\mathbf{E}_v=\begin{pmatrix}0\\ \bar{\tau}_{xx}-\overline{\rho u''u''}\\ \bar{\tau}_{xy}-\overline{\rho u''v''}\\ \bar{\tau}_{xz}-\overline{\rho u''w''}\\ Q_x\end{pmatrix},\quad \mathbf{F}_v=\begin{pmatrix}0\\ \bar{\tau}_{yx}-\overline{\rho v''u''}\\ \bar{\tau}_{yy}-\overline{\rho v''v''}\\ \bar{\tau}_{yz}-\overline{\rho v''w''}\\ Q_y\end{pmatrix},\quad \mathbf{G}_v=\begin{pmatrix}\bar{\tau}_{zx}-\overline{\rho w''u''}\\ \bar{\tau}_{zy}-\overline{\rho w''v''}\\ \bar{\tau}_{zz}-\overline{\rho w''w''}\\ Q_z\end{pmatrix}$$

In the above equations, ρ is the density, u, v, and w are the Cartesian velocity components in x, y and z directions, p is the static pressure, and e is the total energy per unit mass. The overbar denotes the Reynolds-averaged quantity, tilde and double prime denote the Favre mean and Favre fluctuating part of the turbulent motion, respectively. All the flow variables in the above equations are normalized by using the freestream quantities and the reference length L.

Let subscripts 1, 2 and 3 represent the coordinates, x, y, and z, and use Einstein summation convention, the non-dimensional shear stress and Q_x, Q_y, Q_z terms can be expressed in tensor form as

$$\bar{\tau}_{ij}=-\frac{2}{3}\tilde{\mu}\frac{\partial\tilde{u}_k}{\partial x_k}\delta_{ij}+\tilde{\mu}\left(\frac{\partial\tilde{u}_i}{\partial x_j}+\frac{\partial\tilde{u}_j}{\partial x_i}\right) \tag{9}$$

$$Q_i=\tilde{u}_j(\bar{\tau}_{ij}-\overline{\rho u_i''u_j''})-(\bar{q}_i+C_p\overline{\rho T''u_i''}) \tag{10}$$

where the mean molecular heat flux is

$$\bar{q}_i=-\frac{\tilde{\mu}}{(\gamma-1)Pr}\frac{\partial a^2}{\partial x_i} \tag{11}$$

The molecular viscosity $\tilde{\mu}=\tilde{\mu}(\tilde{T})$ is determined by Sutherland law, and $a=\sqrt{\gamma RT_\infty}$ is the speed of sound. The equation of state closes the system

$$\bar{\rho}\tilde{e}=\frac{\tilde{p}}{(\gamma-1)}+\frac{1}{2}\bar{\rho}(\tilde{u}^2+\tilde{v}^2+\tilde{w}^2)+k \tag{12}$$

where γ is the ratio of specific heats, k is the Favre mass-averaged turbulence kinetic energy. The turbulent shear stresses and heat flux appeared in the above equations are calculated by Baldwin–Lomax model [11]. The viscosity is composed of $\mu+\mu_t$, where μ is the molecular

viscosity and μ_t is the turbulent viscosity determined by Baldwin–Lomax model. For a laminar flow, the μ_t is set to be zero. For simplicity, the overbars and tildes are dropped in later analysis.

2.1. Time marching scheme

For the inner flow field domain, the Navier–Stokes equations, Equation (1), are solved implicitly using the control volume method. For steady state solutions, the original Navier–Stokes equations, Equation (1), are solved straightforwardly. For unsteady flow calculations, the dual time-stepping method suggested by Jameson [12] is used with a pseudo-temporal term $\partial\mathbf{Q}/\partial\tau$ added to the governing equations. This term vanishes at the end of each physical time step and has no influence on the accuracy of the solution. However, instead of using the explicit scheme as in Reference [12], an implicit pseudo-time-marching scheme using line Gauss–Seidel iteration is employed to achieve high CPU efficiency. For unsteady time accurate computations, the temporal term is discretized implicitly using a three point, backward differencing as follows:

$$\frac{\partial \mathbf{Q}}{\partial t} = \frac{3Q^{n+1} - 4Q^n + Q^{n-1}}{2\Delta t} \tag{13}$$

where n is the time level index. The pseudo-temporal term is discretized with first-order Euler scheme. Let m stand for the iteration index within a physical time step, the semi-discretized governing equation (Equation (1)) can be expressed as

$$\left[\left(\frac{1}{\Delta\tau} + \frac{1.5}{\Delta t}\right) I - \left(\frac{\partial R}{\partial Q}\right)^{n+1,m}\right] \delta Q^{n+1,m+1} = R^{n+1,m} - \frac{3Q^{n+1,m} - 4Q^n + Q^{n-1}}{2\Delta t} \tag{14}$$

where the $\Delta\tau$ is the pseudo-time-step, R is the net flux going through the control volume

$$R = -\frac{1}{V}\int_s \left[\left(\mathbf{E}' - \frac{1}{Re}\mathbf{E}'_v\right)\mathbf{i} + \left(\mathbf{F}' - \frac{1}{Re}\mathbf{F}'_v\right)\mathbf{j} + \left(\mathbf{G}' - \frac{1}{Re}\mathbf{G}'_v\right)\mathbf{k}\right] \mathrm{d}\mathbf{s} \tag{15}$$

where V is the volume of the control volume, $\mathbf{s}$ is the control volume surface area vector. Equation (14) is solved using the unfactored line Gauss–Seidel iteration. The method can reach very large pseudo-time-step since no factorization error is introduced.

To resolve the shock wave and wall boundary layer with high accuracy, the Roe scheme [13] is employed to evaluate the inviscid fluxes with the third-order MUSCL-type differencing [14]. Central differencing is used for the calculation of viscous fluxes.

3. CHARACTERISTIC FORM OF THE NAVIER–STOKES EQUATIONS

The characteristic form of the Navier–Stokes equations in the generalized coordinates will be solved to determine the NRBC at the phantom cells. To describe the derivation process, the ξ direction will be taken as an example. For the other two directions, the formulations can follow the same procedure and the general formulations are given in the appendix. Based on the strategy of Thompson [7] and Poinsot and Lele [1], the Navier–Stokes equations are expressed first using primitive variables as follows:

$$\mathbf{M}\frac{\partial \mathbf{q}}{\partial t} + \mathbf{A}\cdot\mathbf{M}\frac{\partial \mathbf{q}}{\partial \xi} + \mathbf{B}\cdot\mathbf{M}\frac{\partial \mathbf{q}}{\partial \eta} + \mathbf{C}\cdot\mathbf{M}\frac{\partial \mathbf{q}}{\partial \zeta} = \mathbf{R}_v \tag{16}$$

where $\mathbf{A}, \mathbf{B}, \mathbf{C}$ are the Jacobian matrix

$$\mathbf{A} = \frac{\partial \mathbf{E}'}{\partial \mathbf{Q}'}, \quad \mathbf{B} = \frac{\partial \mathbf{F}'}{\partial \mathbf{Q}'}, \quad \mathbf{C} = \frac{\partial \mathbf{G}'}{\partial \mathbf{Q}'} \tag{17}$$

where $\mathbf{R}_v$ is the viscous vector on the right-hand side of the Navier–Stokes equations, (Equation (1)), $\mathbf{q}$ is the primitive variable vector:

$$\mathbf{q} = \frac{1}{J} \begin{pmatrix} \rho \\ u \\ v \\ w \\ p \end{pmatrix} \tag{18}$$

$\mathbf{M}$ is the Jacobian matrix between the conservative variables and primitive variables

$$\mathbf{M} = \frac{\partial \mathbf{Q}'}{\partial \mathbf{q}} = \begin{pmatrix} 1 & 0 & 0 & 0 & 0 \\ u & \rho & 0 & 0 & 0 \\ v & 0 & \rho & 0 & 0 \\ w & 0 & 0 & \rho & 0 \\ \dfrac{\Phi}{\gamma - 1} & \rho u & \rho v & \rho w & \dfrac{1}{\gamma - 1} \end{pmatrix} \tag{19}$$

where $\Phi = [(\gamma - 1)/2](u^2 + v^2 + w^2)$.

Equation (16) can be further expressed as

$$\frac{\partial \mathbf{q}}{\partial t} + \mathbf{a} \frac{\partial \mathbf{q}}{\partial \xi} + \mathbf{b} \frac{\partial \mathbf{q}}{\partial \eta} + \mathbf{c} \frac{\partial \mathbf{q}}{\partial \zeta} = \mathbf{M}^{-1} \mathbf{R}_v \tag{20}$$

where

$$\mathbf{a} = \mathbf{M}^{-1} \mathbf{A} \mathbf{M}, \quad \mathbf{b} = \mathbf{M}^{-1} \mathbf{B} \mathbf{M}, \quad \mathbf{c} = \mathbf{M}^{-1} \mathbf{C} \mathbf{M} \tag{21}$$

$$\mathbf{M}^{-1} = \begin{pmatrix} 1 & 0 & 0 & 0 & 0 \\ -\dfrac{u}{\rho} & \dfrac{1}{\rho} & 0 & 0 & 0 \\ -\dfrac{v}{\rho} & 0 & \dfrac{1}{\rho} & 0 & 0 \\ -\dfrac{w}{\rho} & 0 & 0 & \dfrac{1}{\rho} & 0 \\ \Phi & -u(\gamma - 1) & -v(\gamma - 1) & -w(\gamma - 1) & \gamma - 1 \end{pmatrix} \tag{22}$$

Matrix $\mathbf{a},\mathbf{b},\mathbf{c}$ have the same eigenvalues as Jacobian matrix $\mathbf{A},\mathbf{B},\mathbf{C}$. In ξ direction,

$$\mathbf{a}=\begin{pmatrix} U & \rho\xi_x & \rho\xi_y & \rho\xi_z & 0 \\ 0 & U & 0 & 0 & \dfrac{\xi_x}{\rho} \\ 0 & 0 & U & 0 & \dfrac{\xi_y}{\rho} \\ 0 & 0 & 0 & U & \dfrac{\xi_z}{\rho} \\ 0 & \gamma p\xi_x & \gamma p\xi_y & \gamma p\xi_z & U \end{pmatrix} \tag{23}$$

where $U=\xi_x u+\xi_y v+\xi_z w$. Matrix $\mathbf{a}$ can also be expressed as

$$\mathbf{a}=\mathbf{P}\mathbf{\Lambda}\mathbf{P}^{-1} \tag{24}$$

where $\mathbf{\Lambda}$ is the eigenvalue matrix, $\mathbf{P}$ is eigenvector matrix of $\mathbf{a}$, and $\mathbf{P}^{-1}$ is the inverse of $\mathbf{P}$. They are given as follows:

$$\mathbf{\Lambda}=\begin{pmatrix} U & 0 & 0 & 0 & 0 \\ 0 & U & 0 & 0 & 0 \\ 0 & 0 & U & 0 & 0 \\ 0 & 0 & 0 & U+C & 0 \\ 0 & 0 & 0 & 0 & U-C \end{pmatrix} \tag{25}$$

$$\mathbf{P}=\begin{pmatrix} \tilde{\xi}_x & \tilde{\xi}_y & \tilde{\xi}_z & \alpha & \alpha \\ 0 & -\tilde{\xi}_z & \tilde{\xi}_y & \tilde{\xi}_x/\sqrt{2} & -\tilde{\xi}_x/\sqrt{2} \\ \tilde{\xi}_z & 0 & -\tilde{\xi}_x & \tilde{\xi}_y/\sqrt{2} & -\tilde{\xi}_y/\sqrt{2} \\ -\tilde{\xi}_y & \tilde{\xi}_x & 0 & \tilde{\xi}_z/\sqrt{2} & -\tilde{\xi}_z/\sqrt{2} \\ 0 & 0 & 0 & \alpha c^2 & \alpha c^2 \end{pmatrix} \tag{26}$$

$$\mathbf{P}^{-1}=\begin{pmatrix} \tilde{\xi}_x & 0 & \tilde{\xi}_z & -\tilde{\xi}_y & -\tilde{\xi}_x/c^2 \\ \tilde{\xi}_y & -\tilde{\xi}_z & 0 & \tilde{\xi}_x & -\tilde{\xi}_y/c^2 \\ \tilde{\xi}_z & \tilde{\xi}_y & -\tilde{\xi}_x & 0 & -\tilde{\xi}_z/c^2 \\ 0 & \tilde{\xi}_x/\sqrt{2} & \tilde{\xi}_y/\sqrt{2} & \tilde{\xi}_z/\sqrt{2} & \beta \\ 0 & -\tilde{\xi}_x/\sqrt{2} & -\tilde{\xi}_y/\sqrt{2} & -\tilde{\xi}_z/\sqrt{2} & \beta \end{pmatrix} \tag{27}$$

where $C = c|\nabla\xi|$, $|\nabla\xi| = \sqrt{{\xi_x}^2 + {\xi_y}^2 + {\xi_z}^2}$, $\tilde{\xi}_x = \xi_x/|\nabla\xi|$, $\tilde{\xi}_y = \xi_y/|\nabla\xi|$, $\tilde{\xi}_z = \xi_z/|\nabla\xi|$, $\alpha = \rho/\sqrt{2}c$, $\beta = 1/\sqrt{2}\rho c$, c is the speed of sound and determined by $c = \sqrt{\gamma RT}$.

The Navier–Stokes equation, Equation (20) then can be expressed as

$$\frac{\partial \mathbf{q}}{\partial t} + \mathbf{P}\mathbf{\Lambda}\mathbf{P}^{-1}\frac{\partial \mathbf{q}}{\partial \xi} + \mathbf{b}\frac{\partial \mathbf{q}}{\partial \eta} + \mathbf{c}\frac{\partial \mathbf{q}}{\partial \zeta} = \mathbf{M}^{-1}\mathbf{R}_v \tag{28}$$

or

$$\mathbf{P}^{-1}\frac{\partial \mathbf{q}}{\partial t} + \mathbf{\Lambda}\mathbf{P}^{-1}\frac{\partial \mathbf{q}}{\partial \xi} + \mathbf{P}^{-1}\mathbf{b}\frac{\partial \mathbf{q}}{\partial \eta} + \mathbf{P}^{-1}\mathbf{c}\frac{\partial \mathbf{q}}{\partial \zeta} = \mathbf{P}^{-1}\mathbf{M}^{-1}\mathbf{R}_v \tag{29}$$

This is the characteristic form of the Navier–Stokes equations in ξ direction. Define vector $\mathscr{L}$ as

$$\mathscr{L} = \mathbf{\Lambda}\mathbf{P}^{-1}\frac{\partial \mathbf{q}}{\partial \xi} \tag{30}$$

The Navier–Stokes equations (Equation (29)) are then expressed as

$$\mathbf{P}^{-1}\frac{\partial \mathbf{q}}{\partial t} + \mathscr{L} + \mathbf{P}^{-1}\mathbf{b}\frac{\partial \mathbf{q}}{\partial \eta} + \mathbf{P}^{-1}\mathbf{c}\frac{\partial \mathbf{q}}{\partial \zeta} = \mathbf{P}^{-1}\mathbf{M}^{-1}\mathbf{R}_v \tag{31}$$

Vector $\mathscr{L}$ is given as follows:

$$\mathscr{L} = \begin{pmatrix} \mathscr{L}_1 \\ \mathscr{L}_2 \\ \mathscr{L}_3 \\ \mathscr{L}_4 \\ \mathscr{L}_5 \end{pmatrix} = \begin{pmatrix} U\left[\tilde{\xi}_x\frac{\partial}{\partial\xi}\left(\frac{\rho}{J}\right) + \tilde{\xi}_z\frac{\partial}{\partial\xi}\left(\frac{v}{J}\right) - \tilde{\xi}_y\frac{\partial}{\partial\xi}\left(\frac{w}{J}\right) - \frac{\tilde{\xi}_x}{c^2}\frac{\partial}{\partial\xi}\left(\frac{p}{J}\right)\right] \\ U\left[\tilde{\xi}_y\frac{\partial}{\partial\xi}\left(\frac{\rho}{J}\right) - \tilde{\xi}_z\frac{\partial}{\partial\xi}\left(\frac{u}{J}\right) + \tilde{\xi}_x\frac{\partial}{\partial\xi}\left(\frac{w}{J}\right) - \frac{\tilde{\xi}_y}{c^2}\frac{\partial}{\partial\xi}\left(\frac{p}{J}\right)\right] \\ U\left[\tilde{\xi}_z\frac{\partial}{\partial\xi}\left(\frac{\rho}{J}\right) + \tilde{\xi}_y\frac{\partial}{\partial\xi}\left(\frac{u}{J}\right) - \tilde{\xi}_x\frac{\partial}{\partial\xi}\left(\frac{v}{J}\right) - \frac{\tilde{\xi}_z}{c^2}\frac{\partial}{\partial\xi}\left(\frac{p}{J}\right)\right] \\ (U+C)\left[\frac{\tilde{\xi}_x}{\sqrt{2}}\frac{\partial}{\partial\xi}\left(\frac{u}{J}\right) + \frac{\tilde{\xi}_y}{\sqrt{2}}\frac{\partial}{\partial\xi}\left(\frac{v}{J}\right) + \frac{\tilde{\xi}_z}{\sqrt{2}}\frac{\partial}{\partial\xi}\left(\frac{w}{J}\right) + \beta\frac{\partial}{\partial\xi}\left(\frac{p}{J}\right)\right] \\ (U-C)\left[-\frac{\tilde{\xi}_x}{\sqrt{2}}\frac{\partial}{\partial\xi}\left(\frac{u}{J}\right) - \frac{\tilde{\xi}_y}{\sqrt{2}}\frac{\partial}{\partial\xi}\left(\frac{v}{J}\right) - \frac{\tilde{\xi}_z}{\sqrt{2}}\frac{\partial}{\partial\xi}\left(\frac{w}{J}\right) + \beta\frac{\partial}{\partial\xi}\left(\frac{p}{J}\right)\right] \end{pmatrix} \tag{32}$$

The vector $\mathscr{L}$ is the amplitude of the characteristic waves. If assume $\tilde{\xi}_x = 1, \tilde{\xi}_y = \tilde{\xi}_z = 0$, Equation (32) returns to the corresponding formulations in x direction of the Cartesian coordinates. As pointed out in References [6, 7], for multi-dimensional Navier–Stokes flow equations, Equation (29), the matrix $\mathbf{P}^{-1}$ cannot be absorbed into the partial derivatives because the flow equations does not satisfy Pfaff's condition and the matrix cannot be treated as constants. In other words, it is incorrect to express the characteristic form of the Navier–Stokes equations in the form given in Reference [5, p. 2042] as

$$\frac{\partial \mathbf{R}}{\partial t} + \mathbf{\Lambda}\frac{\partial \mathbf{R}}{\partial \xi} + = \mathbf{P}^{-1} S_v^* \tag{33}$$

The local 1-D wave amplitude defined in Reference [5] following Equation (33) is therefore also erroneous.

To be consistent with the governing equations of the flow field within inner domain and facilitate programming, it is desirable to express Equation (31) in terms of conservative variables. Multiply Equation (31) by matrix $\mathbf{M} \cdot \mathbf{P}$, the characteristic Navier–Stokes equations expressed in terms of conservative variables in ξ direction is

$$\frac{\partial \mathbf{Q}'}{\partial t} + \mathbf{M}\mathbf{P}\mathscr{L} + \frac{\partial \mathbf{F}'}{\partial \eta} + \frac{\partial \mathbf{G}'}{\partial \zeta} = \frac{1}{Re}\left(\frac{\partial \mathbf{E}_v'}{\partial \xi} + \frac{\partial \mathbf{F}_v'}{\partial \eta} + \frac{\partial \mathbf{G}_v'}{\partial \zeta}\right) \tag{34}$$

Define vector $\mathbf{d}$ as

$$\mathbf{d} = \mathbf{P}\mathscr{L} = \begin{pmatrix} d_1 \\ d_2 \\ d_3 \\ d_4 \\ d_5 \end{pmatrix} = \begin{pmatrix} \tilde{\xi}_x \mathscr{L}_1 + \tilde{\xi}_y \mathscr{L}_2 + \tilde{\xi}_z \mathscr{L}_3 + \alpha(\mathscr{L}_4 + \mathscr{L}_5) \\ -\tilde{\xi}_z \mathscr{L}_2 + \tilde{\xi}_y \mathscr{L}_3 + \dfrac{\tilde{\xi}_x}{\sqrt{2}}(\mathscr{L}_4 - \mathscr{L}_5) \\ \tilde{\xi}_z \mathscr{L}_1 - \tilde{\xi}_x \mathscr{L}_3 + \dfrac{\tilde{\xi}_y}{\sqrt{2}}(\mathscr{L}_4 - \mathscr{L}_5) \\ -\tilde{\xi}_y \mathscr{L}_1 - \tilde{\xi}_x \mathscr{L}_2 + \dfrac{\tilde{\xi}_z}{\sqrt{2}}(\mathscr{L}_4 - \mathscr{L}_5) \\ \alpha c^2(\mathscr{L}_4 + \mathscr{L}_5) \end{pmatrix} \tag{35}$$

Define vector $\mathscr{D}$ as

$$\mathscr{D} = \mathbf{M}\mathbf{d} = \begin{pmatrix} d_1 \\ ud_1 + \rho d_2 \\ vd_1 + \rho d_3 \\ wd_1 + \rho d_4 \\ \dfrac{1}{2}(u^2 + v^2 + w^2)d_1 + \rho u d_2 + \rho v d_3 + \rho w d_4 + \dfrac{1}{\gamma - 1} d_5 \end{pmatrix} \tag{36}$$

Finally, the characteristic form Navier–Stokes equations in conservative form and generalized coordinates in ξ direction can be expressed as

$$\frac{\partial \mathbf{Q}'}{\partial t} + \mathscr{D} + \frac{\partial \mathbf{F}'}{\partial \eta} + \frac{\partial \mathbf{G}'}{\partial \zeta} = \frac{1}{Re}\left(\frac{\partial \mathbf{E}'_v}{\partial \xi} + \frac{\partial \mathbf{F}'_v}{\partial \eta} + \frac{\partial \mathbf{G}'_v}{\partial \zeta}\right) \tag{37}$$

Equation (37) will be solved to determine the NRBC in ξ direction. The Navier–Stokes equations in generalized coordinates and their characteristic forms in η and ζ directions can be obtained straightforwardly following the symmetric rule and are given in the appendix.

By neglecting the transverse and viscous terms in Equation (37), the LODI relation [1] in generalized coordinates is

$$\frac{\partial \mathbf{Q}'}{\partial t} + \mathscr{D} = 0 \tag{38}$$

The LODI relation may be used to estimate the amplitudes of the characteristic waves at boundaries. Numerical results show that the LODI relations works well for the boundaries where the flow fields are smooth or uniform, and hence the transverse and viscous terms are small or negligible. For those boundaries where the transverse and viscous terms are significant, the LODI relations may perform poorly.

4. NON-REFLECTIVE BOUNDARY CONDITIONS

Following the strategy suggested by Poinsot and Lele [1], the characteristic boundary conditions for Navier–Stokes equations can be implemented based on Equation (37). In the present study, Equation (37) is solved implicitly at the phantom cells in a fully coupled manner with the Navier–Stokes equations governing the inner flow field. For unsteady solutions, the dual time-stepping method is used. The semi-discretized equation for Equation (37) is

$$\begin{aligned}\left[\left(\frac{1}{\Delta\tau} + \frac{1.5}{\Delta t}\right) I - \left(\frac{\partial R_{\mathrm{bc}}}{\partial Q}\right)^{n+1,m} + \left(\frac{\partial \mathscr{D}}{\partial Q}\right)^{n+1,m}\right] \delta Q^{n+1,m+1} \\ = R_{\mathrm{bc}}^{n+1,m} - \mathscr{D}^{n+1,m} - \frac{3Q^{n+1,m} - 4Q^n + Q^{n-1}}{2\Delta t}\end{aligned} \tag{39}$$

where

$$R_{\mathrm{bc}} = -\frac{1}{V}\int_s \left[\left(-\frac{1}{Re}\mathbf{E}'_v\right)\mathbf{i} + \left(\mathbf{F}' - \frac{1}{Re}\mathbf{F}'_v\right)\mathbf{j} + \left(\mathbf{G}' - \frac{1}{Re}\mathbf{G}'_v\right)\mathbf{k}\right] \mathbf{ds} \tag{40}$$

Compare Equations (40) and (15), it is noted that in R_{bc}, there is no $\mathbf{E}'$ flux, which is replaced by vector $\mathscr{D}$. Here $\mathscr{D}$ is treated as a source term.

Before proceeding to the further analysis, some notations need to be defined. For the finite volume method used in the present study, a row of phantom cells are used outside of the boundary. The boundary conditions are enforced by assigning values to the primitive variables at those phantom cells. All the variables marked by the subscript 'o' are for phantom cells. The variables at the interior cells adjacent to a boundary are denoted by subscript 'i'.

Equation (37) provides the set of governing equations for NRBC, but the way to implement the NRBC is not unique. The following is the method used in this study and should not be considered as the only feasible method.

4.1. Supersonic outflow boundary conditions

For supersonic flow at exit, all the eigenvalues in Equation (25) are positive and the disturbance propagates from inner domain to outside. The wave amplitude vector, Equation (32) is evaluated using one-side upwind differencing. For supersonic flow at exit, using simple extrapolation may not generate physical wave reflection, but may still generate numerical wave reflection [1]. Solving Equation (39) would achieve a more accurate NRBC for the supersonic flow. For supersonic flow, the exit boundary conditions, ρ_o, ρu_o, ρv_o, ρw_o and ρe_o are completely determined by solving the Navier–Stokes equations in the characteristic form.

To evaluate the derivatives in vector $\mathscr{L}$, either the first- or second-order upwind differencing may be used. For the present study, all the partial derivatives in vector $\mathscr{L}$ are calculated by first-order upwind differencing.

4.2. Subsonic outflow boundary conditions

For subsonic flow at exit, the eigenvalue $U - C$ is negative and the disturbance propagates into the domain from outside. $\mathscr{L}_1$–$\mathscr{L}_4$ can be still calculated by one-side upwind differencing. However, $\mathscr{L}_5$ corresponding to the eigenvalue of $U - C$ must be treated differently. The commonly used method to provide a well-posed boundary condition is to impose $p = p_\infty$ at the outflow boundary. This treatment however will create acoustic wave reflections, which may be diffused and eventually disappear when the solution is converged to a steady state solution. For unsteady flows, the wave reflection may contaminate the flow solutions. To avoid wave reflections, the following soft boundary condition was suggested by Rudy and Strikwerda [15] and used by Poinsot and Lele [1].

$$\mathscr{L}_5 = \mathscr{K}(p - p_e) \tag{41}$$

where $\mathscr{K}$ is a constant and is determined by $\mathscr{K} = \sigma(1 - \mathscr{M}^2)c/L$ as given by Poinsot and Lele [1] for Cartesian coordinates. The corresponding form used in the generalized coordinates is

$$\mathscr{K} = \sigma|1 - \mathscr{M}^2|/(\sqrt{2}J\rho L) \tag{42}$$

where $\mathscr{M}$ is the maximum Mach number in the flow field. L is the characteristic length of the domain. c is the speed of sound. The preferred range for constant σ is 0.2–0.5. The absolute value of $1 - \mathscr{M}^2$ is to ensure the term is positive because the maximum Mach number can be greater than 1 in a transonic flow field.

If $\mathscr{L}_5 = 0$, it switches to the 'perfect' NRBC. However, this boundary condition is not well posed and will not lead the solution to the one matching the exit pressure p_∞. Equation (41) assumes that the constant exit pressure p_∞ is imposed at infinity. There exists reflection if $p \neq p_\infty$, which is needed for the well posedness of the numerical solution. For the unsteady problems, Equation (41) will make the mean value of the pressure at the exit very close to p_∞. However, the pressure at the individual control volume may not be exactly equal to p_∞ even though the value of $\mathscr{L}_5$ can be very small. In this sense, Equation (41) may be considered as 'almost NRBC'.

The complete boundary conditions used at the exit are the pressure at infinity for Equation (41) and three zero gradient viscous conditions:

$$\frac{\partial}{\partial \xi}(\xi_x \tau_{xy} + \xi_y \tau_{yy} + \xi_z \tau_{zy}) = 0 \tag{43}$$

$$\frac{\partial}{\partial \xi}(\xi_x \tau_{xz} + \xi_y \tau_{yz} + \xi_z \tau_{zz}) = 0 \tag{44}$$

$$\frac{\partial}{\partial \xi}(\xi_x Q_x + \xi_y Q_y + \xi_z Q_z) = 0 \tag{45}$$

The amplitudes of the outgoing characteristic waves, $\mathscr{L}_1$–$\mathscr{L}_4$ are computed from the interior domain. All the conservative variables at phantom points are obtained by solving the characteristic Navier–Stokes equations, Equation (37). All the transverse and viscous terms in Equation (37) can be evaluated in the same way as the inner domain control volumes. The Roe's Riemann solver is also used for computing fluxes $\mathbf{F}'$ and $\mathbf{G}'$, central differencing is used for fluxes $\mathbf{E}'_v$, $\mathbf{F}'_v$, $\mathbf{G}'_v$. This strategy makes maximum use of the existing code and minimizes the programming work in implementing the boundary conditions.

4.3. Subsonic inflow boundary conditions

At $\xi = 1$ boundary, four characteristic waves, $\mathscr{L}_1$–$\mathscr{L}_4$ are entering the domain while $\mathscr{L}_5$ is leaving the domain. For 3-D open field flow cases, four physical boundary conditions are needed, i.e. u_o, v_o, w_o and ρ_o are set to be constant. Other primitive variables are specified according to the freestream condition. The total energy ρe_o is obtained by solving the energy equation in Equation (37). The outgoing wave $\mathscr{L}_5$ can be estimated by using interior variables. The rest of the waves are evaluated by using the LODI relations, Equation (38). $\mathscr{L}_1$–$\mathscr{L}_4$ can be expressed as

$$\begin{aligned} \mathscr{L}_1 &= -\tilde{\xi}_x \frac{\rho}{\sqrt{2}c}(\mathscr{L}_4 + \mathscr{L}_5), \quad \mathscr{L}_2 = -\tilde{\xi}_y \frac{\rho}{\sqrt{2}c}(\mathscr{L}_4 + \mathscr{L}_5) \\ \mathscr{L}_3 &= -\tilde{\xi}_z \frac{\rho}{\sqrt{2}c}(\mathscr{L}_4 + \mathscr{L}_5), \quad \mathscr{L}_4 = \mathscr{L}_5 \end{aligned} \tag{46}$$

4.4. Adiabatic wall boundary conditions

At a 3-D adiabatic wall ($\eta = \text{constant}$), the no-slip condition is enforced by extrapolating the velocity between the phantom and interior cells, $u_o = -u_i$, $v_o = -v_i$, and $w_o = -w_i$. One more physical boundary condition to be imposed on the wall is the adiabatic condition, $\partial T/\partial \eta = 0$. From the adiabatic condition, the ρ_o can be expressed as follows:

$$\frac{p_o}{\rho_o} = \frac{p_i}{\rho_i} \tag{47}$$

The total energy ρe_o is determined by solving the energy equation in Equation (37). Then using Equations (47) and (12), ρ_o and p_o can be solved. Cross a η boundary, vector $\mathscr{L}$ is expressed as follows:

$$\mathscr{L} = \begin{pmatrix} \mathscr{L}_1 \\ \mathscr{L}_2 \\ \mathscr{L}_3 \\ \mathscr{L}_4 \\ \mathscr{L}_5 \end{pmatrix} = \begin{pmatrix} V\left[\tilde{\eta}_x \frac{\partial}{\partial \eta}\left(\frac{\rho}{J}\right) + \tilde{\eta}_z \frac{\partial}{\partial \eta}\left(\frac{v}{J}\right) - \tilde{\eta}_y \frac{\partial}{\partial \eta}\left(\frac{w}{J}\right) - \frac{\tilde{\eta}_x}{c^2}\frac{\partial}{\partial \eta}\left(\frac{p}{J}\right)\right] \\ V\left[\tilde{\eta}_y \frac{\partial}{\partial \eta}\left(\frac{\rho}{J}\right) - \tilde{\eta}_z \frac{\partial}{\partial \eta}\left(\frac{u}{J}\right) + \tilde{\eta}_x \frac{\partial}{\partial \eta}\left(\frac{w}{J}\right) - \frac{\tilde{\eta}_y}{c^2}\frac{\partial}{\partial \eta}\left(\frac{p}{J}\right)\right] \\ V\left[\tilde{\eta}_z \frac{\partial}{\partial \eta}\left(\frac{\rho}{J}\right) + \tilde{\eta}_y \frac{\partial}{\partial \eta}\left(\frac{u}{J}\right) - \tilde{\eta}_x \frac{\partial}{\partial \eta}\left(\frac{v}{J}\right) - \frac{\tilde{\eta}_z}{c^2}\frac{\partial}{\partial \eta}\left(\frac{p}{J}\right)\right] \\ (V+C)\left[\frac{\tilde{\eta}_x}{\sqrt{2}}\frac{\partial}{\partial \eta}\left(\frac{u}{J}\right) + \frac{\tilde{\eta}_y}{\sqrt{2}}\frac{\partial}{\partial \eta}\left(\frac{v}{J}\right) + \frac{\tilde{\eta}_z}{\sqrt{2}}\frac{\partial}{\partial \eta}\left(\frac{w}{J}\right) + \beta\frac{\partial}{\partial \eta}\left(\frac{p}{J}\right)\right] \\ (V-C)\left[-\frac{\tilde{\eta}_x}{\sqrt{2}}\frac{\partial}{\partial \eta}\left(\frac{u}{J}\right) - \frac{\tilde{\eta}_y}{\sqrt{2}}\frac{\partial}{\partial \eta}\left(\frac{v}{J}\right) - \frac{\tilde{\eta}_z}{\sqrt{2}}\frac{\partial}{\partial \eta}\left(\frac{w}{J}\right) + \beta\frac{\partial}{\partial \eta}\left(\frac{p}{J}\right)\right] \end{pmatrix} \tag{48}$$

where $V = \eta_x u + \eta_y v + \eta_z w$ and $C = c|\nabla\eta|$, $|\nabla\eta| = \sqrt{\eta_x^2 + \eta_y^2 + \eta_z^2}$. It can be seen from Equation (48), the characteristic waves $\mathscr{L}_1$–$\mathscr{L}_3$ vanish since $V = 0$ at wall surface. At lower wall ($\eta = 1$), the outgoing characteristic wave $\mathscr{L}_5$ is computed from the interior domain. The incoming wave $\mathscr{L}_4$ is estimated by using LODI relations. By solving 2nd–4th equations in Equation (38), it yields $\mathscr{L}_4 = \mathscr{L}_5$. At upper wall (maximum η), the $\mathscr{L}_4$ becomes the outgoing wave, and it can be computed from the interior domain. $\mathscr{L}_5$ is the incoming wave which is evaluated by $\mathscr{L}_5 = \mathscr{L}_4$.

5. RESULTS AND DISCUSSION

5.1. A vortex propagating through a outflow boundary

The first test case is a subsonic vortex propagating flow in an open flow field. The computed domain is rectangular inclined 30° about the horizontal axis as a validation for the generalized coordinates. The subsonic inflow and outflow boundary conditions are used at the inlet and exit, and far-field boundaries are used on the upper and lower borders. In Reference [1], a supersonic vortex propagating flow is chosen. It is known that a subsonic vortex propagating flow is more difficult to deal with since the disturbance propagates both upstream and

downstream. To test present method under more general conditions, the subsonic vortex propagating flow is selected for this study.

The computational mesh has a length of 2 units in streamwise direction which is 30° to the x direction, while the width is 4 units in transverse direction. The mesh dimensions are 60×100. The laminar Navier–Stokes equations is solved for this flow with $M = 0.8$ and Reynolds number of 300.

A vorticity is initially located at the centre of the domain when dimensionless time $t^* = 0$, and convected downstream toward the outflow boundary. The velocity flow field is initially specified as

$$\begin{pmatrix} u \\ v \end{pmatrix} = \begin{pmatrix} u_\infty \\ v_\infty \end{pmatrix} + \begin{pmatrix} \dfrac{\partial \psi}{\partial y} \\ -\dfrac{\partial \psi}{\partial x} \end{pmatrix} \tag{49}$$

$$\psi = C_v \exp\left(-\frac{x^2 + y^2}{2R_c^2}\right) \tag{50}$$

where u_∞ and v_∞ are the velocity components of the incoming flow, C_v is the coefficient that determines the vortex strength of the velocity field, and R_c is the vortex radius. The total energy field is initialized as

$$\rho e = \rho e_\infty + \rho \frac{C_e^2}{R_c^2} \exp\left(-\frac{x^2 + y^2}{2R_c^2}\right) \tag{51}$$

where C_e is the coefficient that determines the vortex strength of the total energy field. Equations (49) and (51) are adopted from those used by Poinsot and Lele [1]. The coefficients C_v and C_e, and radius R_c are defined by

$$C_v/(cL) = -0.0005, \quad C_e/(cL) = -0.02, \quad R_c = 0.15 \tag{52}$$

The inflow and outflow boundary conditions used in this case are described in previous section. The far-field upper and lower boundaries are treated as perfect non-reflective outflow boundary.

The flow field at inflow boundary is initially set to be uniform. The direction of the incoming flow is parallel to the constant η lines. Obviously, at the inflow boundary, the transverse flux and viscous terms are very small. The error caused by LODI relations is very small and negligible.

To compare the present NRBC with the commonly used outflow boundary conditions (fixed pressure outflow boundary conditions, FPBC) in which the fixed downstream pressure is imposed for subsonic flow simulations, the first computation is carried out with FPBC, which includes: at inflow boundary, u_o, v_o, ρ_o are given such that the streamwise velocity component is uniformly distributed and the transverse velocity component is equal to zero, the pressure is extrapolated from the interior domain, $p_o = p_i$, then the total energy ρe_o can be computed from the equation of state; at outflow boundary, all the primitive variables are extrapolated from the inner domain except the pressure is set to be constant. The CFL number of the

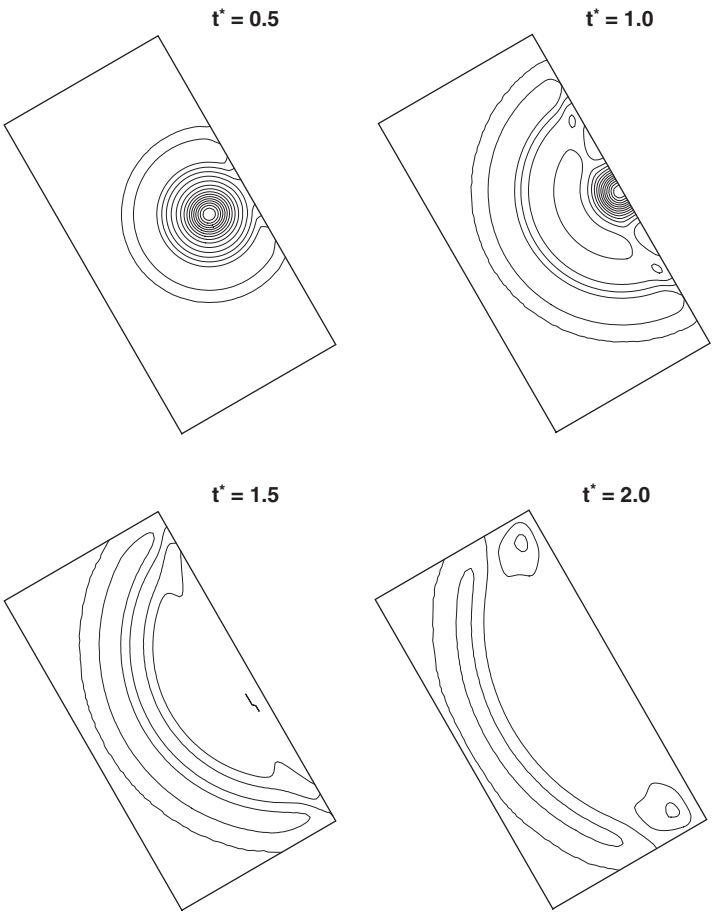

Figure 1. Density contours at four instants for a vortex leaving the domain using imposed exit static pressure boundary conditions.

pseudo-time-step is 500. The estimated physical time step CFL is 0.74, which is determined by the time accuracy of the physical problem.

The same case with the same initial flow condition and same CFL number is then calculated using the NRBC developed in present study. The value of σ in Equation (42) is set to be 0.25. Figures 1 and 2 show the computed density contours at four instants by FPBC and NRBC, respectively. It can be seen from Figure 1 that the flow field is seriously distorted by the reflective waves when the vortex propagates through the exit boundary. But there is no notable distortion in the solution calculated using NRBC as shown in Figure 2. The vortex passes through the outflow NRBC very smoothly. Figures 3 and 4 show the relative streamwise velocity component, $(u^\tau - u^\tau_\infty)/u^\tau_\infty$ contours at the same four instants by FPBC and NRBC, respectively. The same phenomenon is observed. Figure 5 shows the time histories of $|p_{\max} - p_{\min}|$ for the full course of the computation. As can be seen, the level of spurious pressure reflection caused by FPBC is much higher than the one by NRBC.

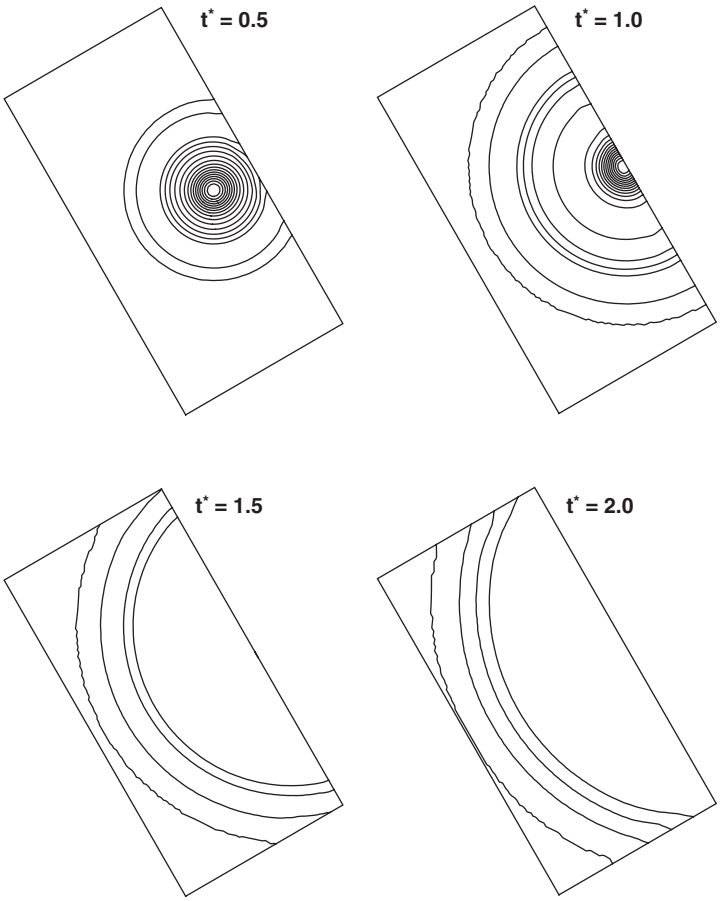

Figure 2. Density contours at four instants for a vortex leaving the domain using NRBC exit boundary conditions.

5.2. *Inlet-diffuser flow*

To test the NRBC for realistic engineering problems. A transonic inlet diffuser with shock wave–boundary layer interaction [16] is computed to demonstrate the advantage of the NRBC.

5.2.1. Steady state solutions. The steady state solution of the inlet diffuser is calculated first to verify that the NRBC is consistent with the steady state flow. The Reynolds number is 3.45×10^5 and the inlet Mach number is 0.46.

The baseline geometry of the inlet diffuser has a height of $H = 4.4\,\text{cm}$ at the throat and a total length of $12.6H$. This case is run using a H-type grid with the dimensions of 110×56. The turbulence shear stress and heat flux are calculated by the Baldwin–Lomax model [11]. The experimental data provided by Bogar *et al.* [16] are available for validation.

As discussed before, for 3-D case, at $\xi = 1$ inlet boundary, waves $\mathscr{L}_1$–$\mathscr{L}_4$ enter the boundary and $\mathscr{L}_5$ leaves. Hence, four physical boundary conditions are required at this boundary.

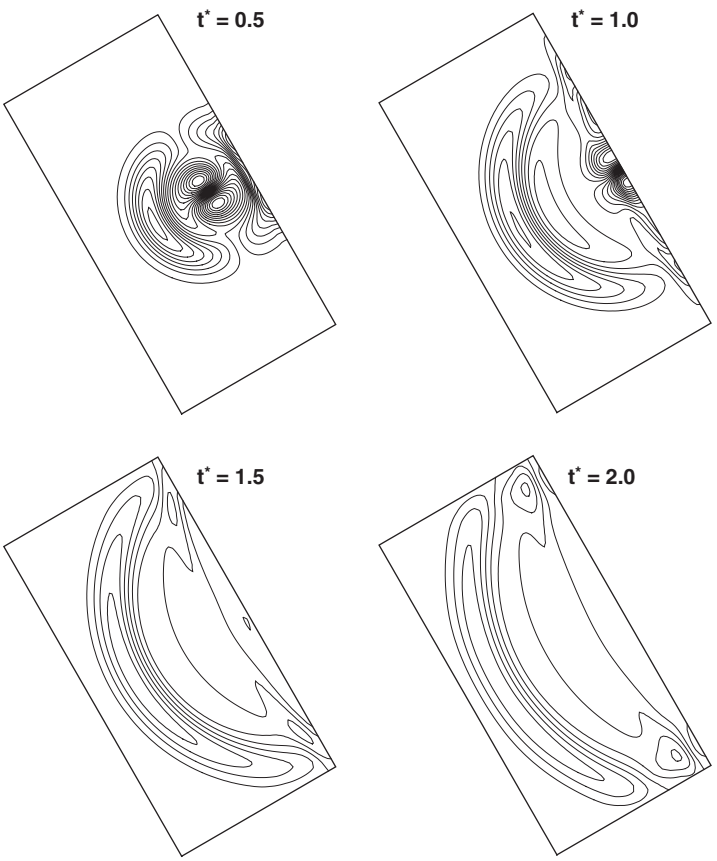

Figure 3. $(u^{\tau} - u^{\tau}_{\infty})/u^{\tau}_{\infty}$ contours at four instants for a vortex leaving the domain using imposed exit static pressure boundary conditions.

The amplitude of the outgoing characteristic wave $\mathscr{L}_5$ can be estimated from the interior points.

According to Poinsot and Lele [1], the inlet and wall NRBC are not as critical as the exit NRBC. For this transonic inlet-diffuser case, at the upstream of the shock, the flow is supersonic. Hence, the perturbation will not propagate upstream. The NRBC at inlet therefore may not be necessary. The conventional boundary condition at inlet is expected to work well. However, at the downstream of the shock, the flow is subsonic. The oscillation of the shock will generate strong reflecting waves at the exit boundary. Therefore, exit NRBC is essential for this case. For this reason, the inflow NRBC is not used in this study. Instead, the inlet BC with given total pressure P_t, total temperature T_t, and flow angle is used. The NRBC outflow and wall conditions used are those described in previous section.

The Mach number contours are shown in Figure 6. Corresponding to different back pressure in the experiment, there are two cases of the flow, one has a weak shock ($p_{\text{outlet}}/p_t = 0.82$) and the other has a strong shock ($p_{\text{outlet}}/p_t = 0.72$). Figures 7 and 8 show the computed static

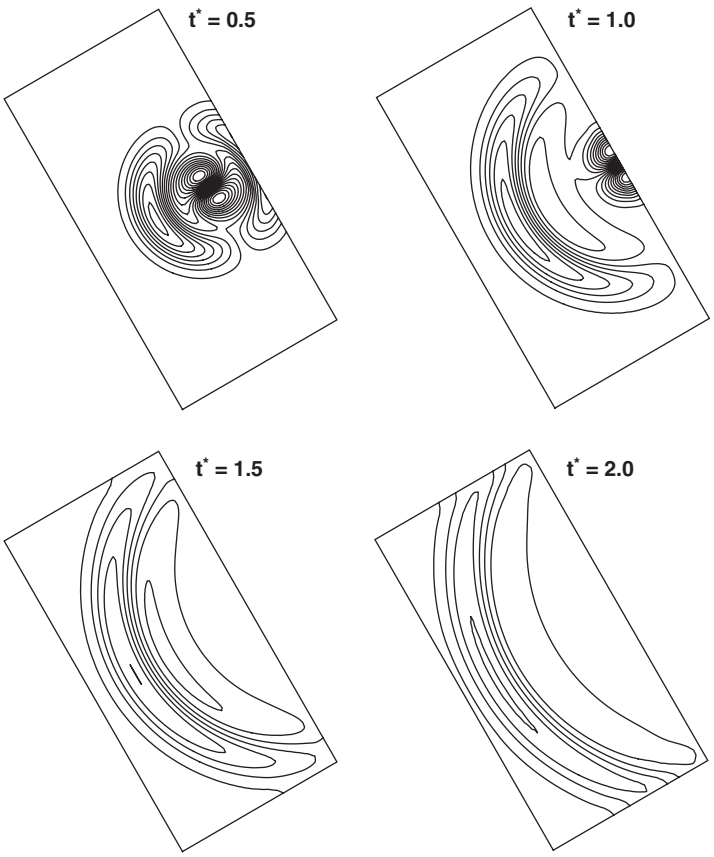

Figure 4. $(u^\tau - u^\tau_\infty)/u^\tau_\infty$ contours at three instants for a vortex leaving the domain using NRBC exit boundary conditions.

pressure distributions compared with the experimental data along the top and bottom wall for the weak shock case. Good agreement is obtained between the computation and experiment.

Figures 9 and 10 show the static pressure distribution compared with the experimental data along the top and bottom walls for the strong shock case. Due to the strong shock interacting with the turbulent boundary layer, there is a flow separation downstream of the shock, which is not well predicted. There may be two reasons for the problem: (1) the flow is unsteady due to the separation and hence the steady state solution cannot capture the separation bubble length correctly; (2) the Baldwin–Lomax turbulence model is inadequate to handle the non-equilibrium separated flow.

Different σ values from 0.1 to 0.35 are tested and the results show that the steady state results are insensitive to the σ value. The fixed pressure boundary conditions are also applied to the same case, and achieve almost the same results as those computed by the NRBC. This is because that, for the steady state solutions, the reflective waves are eventually diffused when the steady state solution is converged.

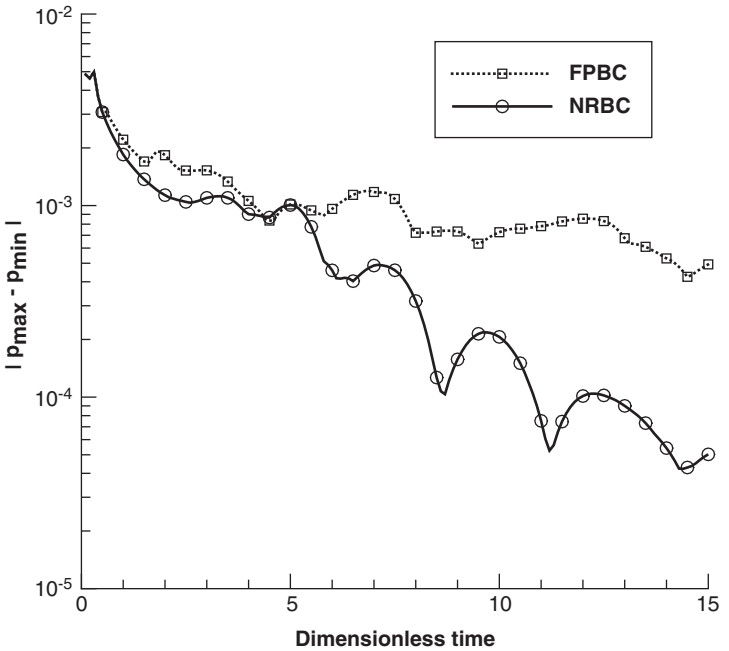

Figure 5. Time histories of $|p_{\max} - p_{\min}|$ for a vortex leaving the domain.

Figure 6. Mach number contours of the inlet diffuser.

5.2.2. Unsteady solutions. The steady state calculation indicates that the NRBC is not essential since the artificial reflective waves are diffused when the solution is converged. However, it is very different when the unsteady flow is calculated. For the inlet-diffuser case with a strong shock wave, the FPBC generates strong reflective waves and makes the shock wave severely oscillating inside the duct. The amplitude of the oscillation is far greater than the experimental results. When the NRBC is applied, the shock oscillation is dramatically reduced.

Figures 11 and 12 show the time-averaged pressure distributions compared with the experimental data. The CFL number of the pseudo-time-step is equal to 5 for all the cases. The estimated CFL number of the physical time step is about 3000, which gives approximately 128 steps in a shock-oscillation cycle of the computed dominant frequency 267 Hz. The value of σ in Equation (42) is 0.25. Due to the large shock oscillation, the shock location is smeared out for the FPBC. Hence, the shock location, strength and the pressure downstream of the shock are poorly predicted. When the NRBC is applied, the reduced shock oscillation yields sharp shock profile and much better agreement of the shock location with the experiment.

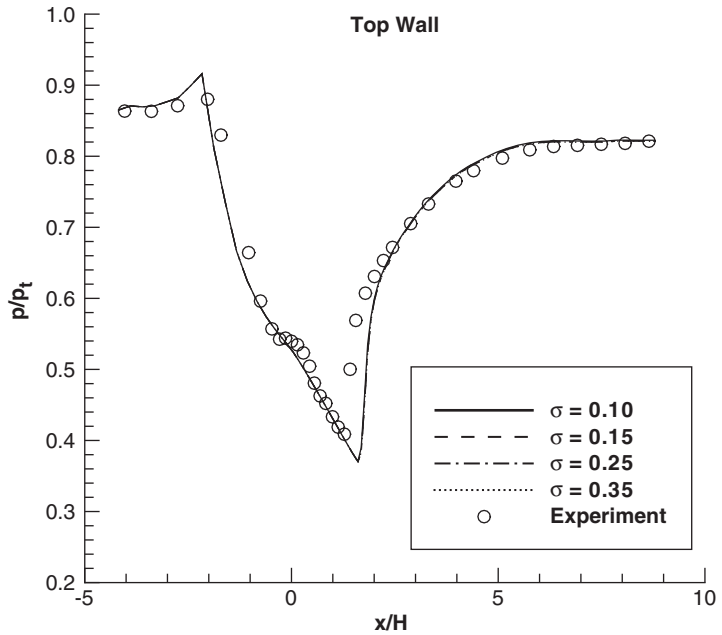

Figure 7. Steady state pressure distribution along the top wall for $p_{\text{outlet}}/p_{\text{t}} = 0.82$.

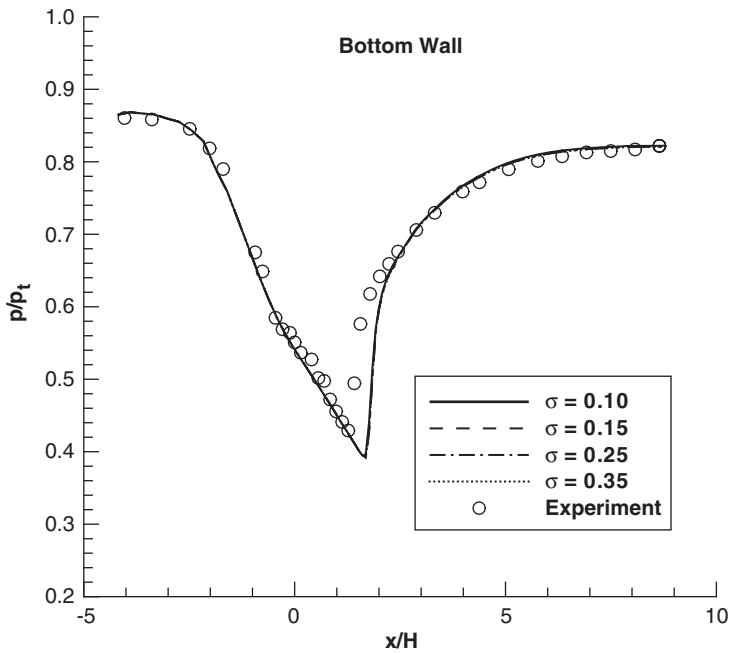

Figure 8. Steady state pressure distribution along the bottom wall for $p_{\text{outlet}}/p_{\text{t}} = 0.82$.

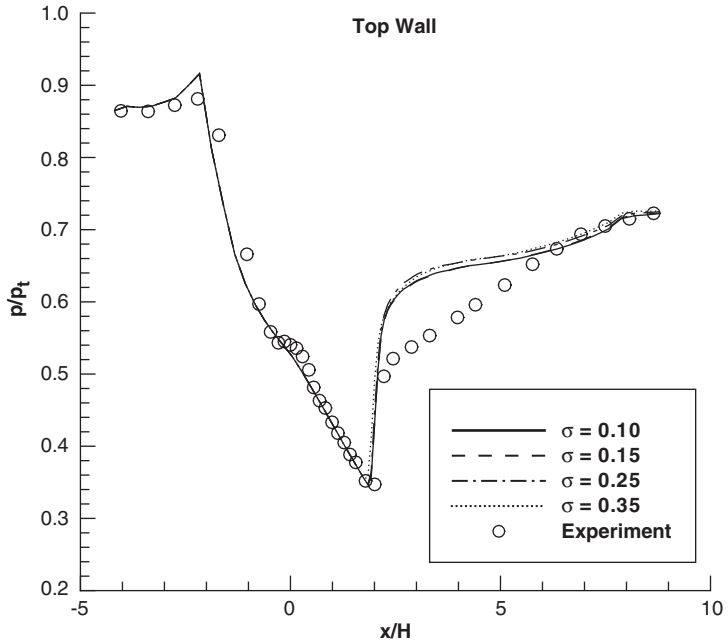

Figure 9. Steady state pressure distribution along the top wall for $p_{\text{outlet}}/p_{\text{t}} = 0.72$.

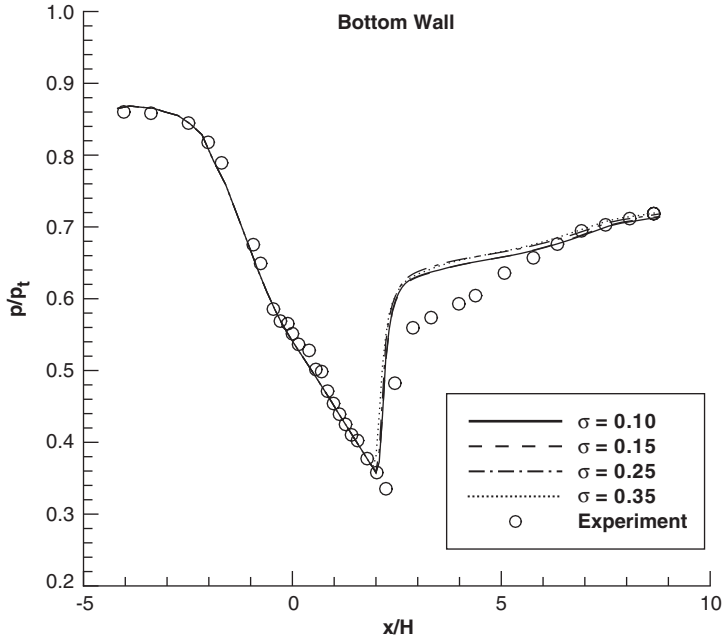

Figure 10. Steady state static pressure distribution along the bottom wall for $p_{\text{outlet}}/p_{\text{t}} = 0.72$.

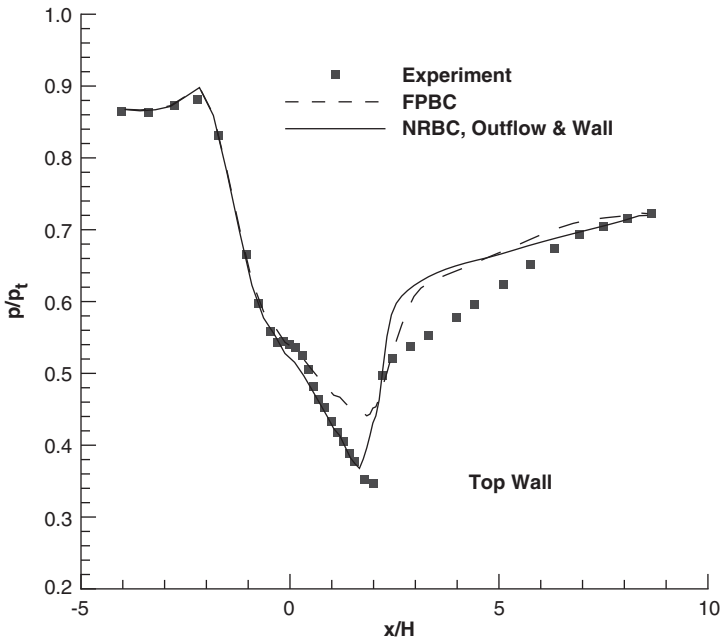

Figure 11. Time-averaged unsteady pressure distribution along the top wall for $p_{\text{outlet}}/p_{\text{t}} = 0.72$.

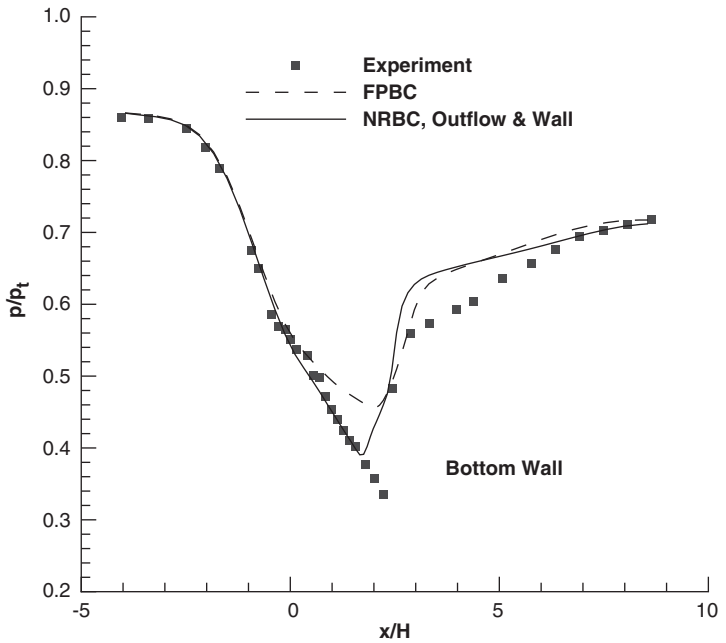

Figure 12. Time-averaged unsteady pressure distribution along the bottom wall for $p_{\text{outlet}}/p_{\text{t}} = 0.72$.

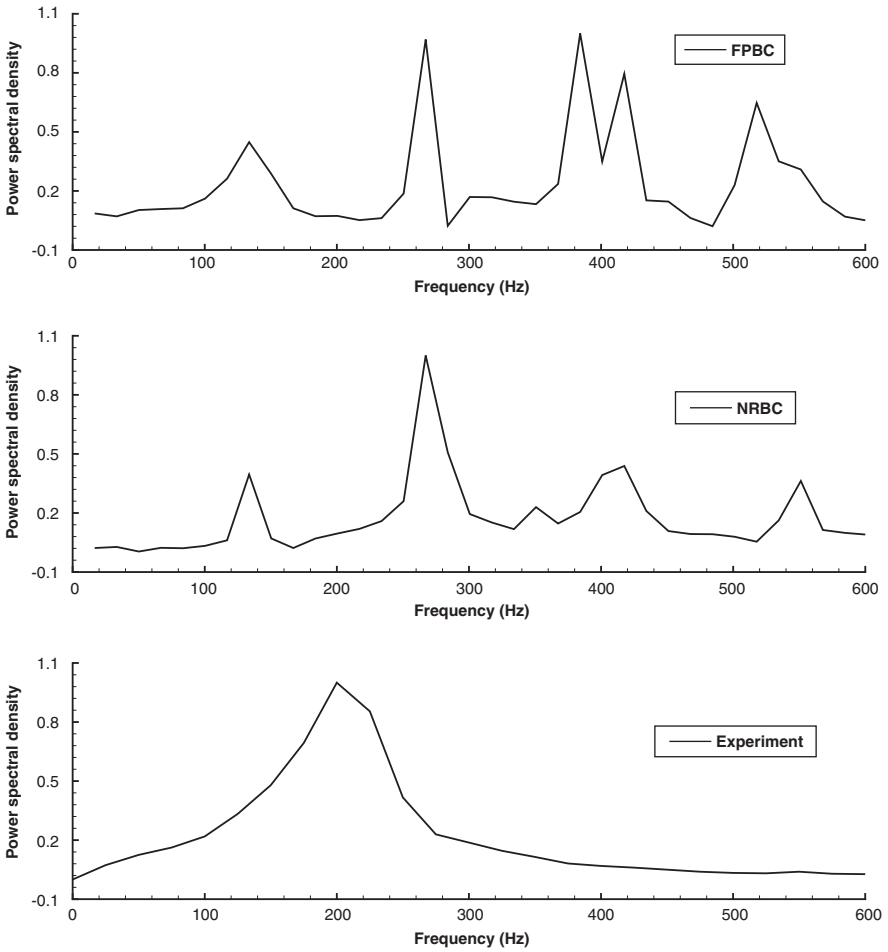

Figure 13. Power spectral density for the static pressure fluctuations at $x/H = 14.218$, $p_{\text{outlet}}/p_{\text{t}} = 0.72$.

To match the experimental geometry for the measured shock-oscillation frequency, the computational domain is then extend to a total length of $21.3H$. The simulation is carried out with FPBC and NRBC, respectively, using the same flow conditions. The computed and experimental power spectra for the static pressure at the exit location ($x/H = 14.218$) are shown in Figure 13. The experimental spectrum (the bottom one) of the shock oscillation measured for this case has one dominant frequency around 200 Hz [16]. The power spectrum computed by NRBC in the middle plot shows that there is only one significantly dominant frequency at about 267 Hz. The power spectrum computed by FPBC in the top plot has the dominant frequency at 384 Hz, which is obviously very different from the dominant frequency of the experimental value of 200 Hz. Obviously, NRBC gives better results than the FPBS does, which is also better than the computed value of 317 Hz predicted by Hsieh *et al.* [17]. It is evident that the NRBC improves the numerical accuracy by reducing the false reflections,

and the noise level created by NRBC is also much lower than the one created by FPBC. The results show that the NRBC is essential to accurately predict unsteady aerodynamic forcing.

6. CONCLUSION

The non-reflective boundary conditions of Poinsot and Lele [1] for 3-D Navier–Stokes equations are extended to the generalized coordinates in this paper. The characteristic form Navier–Stokes equations in conservative variables are given. The NRBC is applied numerically in an implicit time marching method. The governing equations for inner domain and NRBC are solved simultaneously in a fully coupled manner.

For the unsteady subsonic vortex propagating flow, the fixed pressure outflow boundary conditions imposing the exit pressure generates serious wave reflection and the flow field is distorted, whereas, the NRBC developed in this paper generates clean results with no wave reflection and solution distortion.

For the transonic inlet diffuser, the NRBC is not necessary for steady state solutions since the reflective waves are diffused when the solutions are converged. However, for unsteady flows, the NRBC is essential. The FPBC generate strong reflective waves due to the shock–boundary layer interaction, which makes the shock-oscillating motion far greater than the experimental data. When the NRBC is applied, the shock oscillation is dramatically reduced and the computed time-averaged pressure distributions and frequency spectrum agree much better with the experiment than FPBC.

APPENDIX A: CHARACTERISTIC FORM OF THE NAVIER–STOKES EQUATIONS IN A GENERAL DIRECTION

The Navier–Stokes equations in the characteristic form given in the paper is in ξ direction. Assume k is a general direction of ξ, η or ζ, the Characteristic Form of the Navier–Stokes equations in k direction then can be given as

$$\frac{\partial \mathbf{Q}'}{\partial t} + \mathscr{D}_k + \frac{\partial \mathbf{S}'_m}{\partial m} = \mathscr{R}_v \tag{A1}$$

where $\mathbf{S}'_m = \mathbf{E}'$ for $k = \xi$, $\mathbf{S}'_m = \mathbf{F}'$ for $k = \eta$, $\mathbf{S}'_m = \mathbf{G}'$ for $k = \zeta$; m includes the remaining two curvilinear directions other than the k direction. The third term in Equation (A1) is the summation of the two terms in the direction other than the k direction. The viscous vector on the right-hand side of the equation is defined as

$$\mathscr{R}_v = \frac{1}{Re}\left(\frac{\partial \mathbf{E}'_v}{\partial \xi} + \frac{\partial \mathbf{F}'_v}{\partial \eta} + \frac{\partial \mathbf{G}'_v}{\partial \zeta}\right) \tag{A2}$$

The vector $\mathscr{D}_k$ is defined as

$$\mathscr{D}_k = \mathbf{M}\mathbf{P}_k \mathbf{\Lambda}_k \mathbf{P}_k^{-1} \frac{\partial \mathbf{q}}{\partial k} = \mathbf{M}\mathbf{P}_k \mathscr{L}_k = \mathbf{M}\mathbf{d}_k \tag{A3}$$

where $\mathbf{M}$ is the Jacobian matrix between the conservative variables and primitive variables, $\mathbf{\Lambda}_k$ is the eigenvalue matrix, $\mathbf{P}_k$ is eigenvector matrix, and $\mathbf{P}_k^{-1}$ is the inverse of $\mathbf{P}_k$. They are given as follows:

$$\mathbf{M}=\begin{pmatrix} 1 & 0 & 0 & 0 & 0 \\ u & \rho & 0 & 0 & 0 \\ v & 0 & \rho & 0 & 0 \\ w & 0 & 0 & \rho & 0 \\ \dfrac{\Phi}{\gamma-1} & \rho u & \rho v & \rho w & \dfrac{1}{\gamma-1} \end{pmatrix} \tag{A4}$$

$$\mathbf{\Lambda}_k = \begin{pmatrix} \lambda_k^1 & 0 & 0 & 0 & 0 \\ 0 & \lambda_k^2 & 0 & 0 & 0 \\ 0 & 0 & \lambda_k^3 & 0 & 0 \\ 0 & 0 & 0 & \lambda_k^4 & 0 \\ 0 & 0 & 0 & 0 & \lambda_k^5 \end{pmatrix} \tag{A5}$$

$$\mathbf{P}_k=\begin{pmatrix} \tilde{k}_x & \tilde{k}_y & \tilde{k}_z & \alpha & \alpha \\ 0 & -\tilde{k}_z & \tilde{k}_y & \tilde{k}_x/\sqrt{2} & -\tilde{k}_x/\sqrt{2} \\ \tilde{k}_z & 0 & -\tilde{k}_x & \tilde{k}_y/\sqrt{2} & -\tilde{k}_y/\sqrt{2} \\ -\tilde{k}_y & \tilde{k}_x & 0 & \tilde{k}_z/\sqrt{2} & -\tilde{k}_z/\sqrt{2} \\ 0 & 0 & 0 & \alpha c^2 & \alpha c^2 \end{pmatrix} \tag{A6}$$

$$\mathbf{P}_k^{-1} = \begin{pmatrix} \tilde{k}_x & 0 & \tilde{k}_z & -\tilde{k}_y & -\tilde{k}_x/c^2 \\ \tilde{k}_y & -\tilde{k}_z & 0 & \tilde{k}_x & -\tilde{k}_y/c^2 \\ \tilde{k}_z & \tilde{k}_y & -\tilde{k}_x & 0 & -\tilde{k}_z/c^2 \\ 0 & \tilde{k}_x/\sqrt{2} & \tilde{k}_y/\sqrt{2} & \tilde{k}_z/\sqrt{2} & \beta \\ 0 & -\tilde{k}_x/\sqrt{2} & -\tilde{k}_y/\sqrt{2} & -\tilde{k}_z/\sqrt{2} & \beta \end{pmatrix} \tag{A7}$$

where $\Phi = \frac{\gamma-1}{2}(u^2+v^2+w^2)$, $\lambda_k^1 = \lambda_k^2 = \lambda_k^3 = k_x u + k_y v + k_z w = \theta_k$, $\lambda_k^4 = \theta_k + c|\nabla k|$, $\lambda_k^5 = \theta_k - c|\nabla k|$, $|\nabla k| = \sqrt{k_x^2 + k_y^2 + k_z^2}$, $\tilde{k}_x = k_x/|\nabla k|$, $\tilde{k}_y = k_y/|\nabla k|$, $\tilde{k}_z = k_z/|\nabla k|$, $\alpha = \rho/\sqrt{2}c$, $\beta = 1/\sqrt{2}\rho c$, and c is the speed of sound.

The amplitude of the characteristic waves $\mathscr{L}$ is given as follows:

$$\mathscr{L}_k = \begin{pmatrix} \mathscr{L}_k^1 \\ \mathscr{L}_k^2 \\ \mathscr{L}_k^3 \\ \mathscr{L}_k^4 \\ \mathscr{L}_k^5 \end{pmatrix} = \begin{pmatrix} \theta_k \left[\tilde{k}_x \frac{\partial}{\partial k}\left(\frac{\rho}{J}\right) + \tilde{k}_z \frac{\partial}{\partial k}\left(\frac{v}{J}\right) - \tilde{k}_y \frac{\partial}{\partial k}\left(\frac{w}{J}\right) - \frac{\tilde{k}_x}{c^2}\frac{\partial}{\partial k}\left(\frac{p}{J}\right) \right] \\ \theta_k \left[\tilde{k}_y \frac{\partial}{\partial k}\left(\frac{\rho}{J}\right) - \tilde{k}_z \frac{\partial}{\partial k}\left(\frac{u}{J}\right) + \tilde{k}_x \frac{\partial}{\partial k}\left(\frac{w}{J}\right) - \frac{\tilde{k}_y}{c^2}\frac{\partial}{\partial k}\left(\frac{p}{J}\right) \right] \\ \theta_k \left[\tilde{k}_z \frac{\partial}{\partial k}\left(\frac{\rho}{J}\right) + \tilde{k}_y \frac{\partial}{\partial k}\left(\frac{u}{J}\right) - \tilde{k}_x \frac{\partial}{\partial k}\left(\frac{v}{J}\right) - \frac{\tilde{k}_z}{c^2}\frac{\partial}{\partial k}\left(\frac{p}{J}\right) \right] \\ (\theta_k + c|\nabla k|) \left[\frac{\tilde{k}_x}{\sqrt{2}} \frac{\partial}{\partial k}\left(\frac{u}{J}\right) + \frac{\tilde{k}_y}{\sqrt{2}} \frac{\partial}{\partial k}\left(\frac{v}{J}\right) + \frac{\tilde{k}_z}{\sqrt{2}} \frac{\partial}{\partial k}\left(\frac{w}{J}\right) + \beta \frac{\partial}{\partial k}\left(\frac{p}{J}\right) \right] \\ (\theta_k - c|\nabla k|) \left[-\frac{\tilde{k}_x}{\sqrt{2}} \frac{\partial}{\partial k}\left(\frac{u}{J}\right) - \frac{\tilde{k}_y}{\sqrt{2}} \frac{\partial}{\partial k}\left(\frac{v}{J}\right) - \frac{\tilde{k}_z}{\sqrt{2}} \frac{\partial}{\partial k}\left(\frac{w}{J}\right) + \beta \frac{\partial}{\partial k}\left(\frac{p}{J}\right) \right] \end{pmatrix} \tag{A8}$$

Define vector $\mathbf{d}$ as

$$\mathbf{d} = \mathbf{P}_k \mathscr{L}_k = \begin{pmatrix} d_k^1 \\ d_k^2 \\ d_k^3 \\ d_k^4 \\ d_k^5 \end{pmatrix} = \begin{pmatrix} \tilde{k}_x \mathscr{L}_k^1 + \tilde{k}_y \mathscr{L}_k^2 + \tilde{k}_z \mathscr{L}_k^3 + \alpha(\mathscr{L}_k^4 + \mathscr{L}_k^5) \\ -\tilde{k}_z \mathscr{L}_k^2 + \tilde{k}_y \mathscr{L}_k^3 + \frac{\tilde{k}_x}{\sqrt{2}}(\mathscr{L}_k^4 - \mathscr{L}_k^5) \\ \tilde{k}_z \mathscr{L}_k^1 - \tilde{k}_x \mathscr{L}_k^3 + \frac{\tilde{k}_y}{\sqrt{2}}(\mathscr{L}_k^4 - \mathscr{L}_k^5) \\ -\tilde{k}_y \mathscr{L}_k^1 - \tilde{k}_x \mathscr{L}_k^2 + \frac{\tilde{k}_z}{\sqrt{2}}(\mathscr{L}_k^4 - \mathscr{L}_k^5) \\ \alpha c^2 (\mathscr{L}_k^4 + \mathscr{L}_k^5) \end{pmatrix} \tag{A9}$$

Define vector $\mathscr{D}_k$ as

$$\mathscr{D}_k = \mathbf{M}\mathbf{d}_k = \begin{pmatrix} d_k^1 \\ ud_k^1 + \rho d_k^2 \\ vd_k^1 + \rho d_k^3 \\ wd_k^1 + \rho d_k^4 \\ \frac{1}{2}(u^2+v^2+w^2)d_k^1 + \rho u d_k^2 + \rho v d_k^3 + \rho w d_k^4 + \frac{1}{\gamma-1}d_k^5 \end{pmatrix} \tag{A10}$$

ACKNOWLEDGEMENTS

This work is supported by AFOSR Grant F49620-03-1-0253 monitored by Dr Fariba Fahroo.

REFERENCES

1. Poinsot TJ, Lele SK. Boundary conditions for direct simulations of compressible viscous flows. *Journal of Computational Physics* 1992; **101**:104–129.
2. Nishizawa T, Takata H. Numerical study on rotating stall in finite pitch cascades. *ASME Paper*, *Proceedings of the International Gas Turbine and Aeroengine Congress and Exposition*, The Hague, Netherlands, June 1994.
3. He L. Computational study of rotating stall inception in axial compressors. *Journal of Propulsion and Power* 1997; **13**:31–38.
4. Giles MB. Nonreflecting boundary conditions for Euler calculations. *AIAA Journal* 1990; **28**(12):2050–2058.
5. Kim JW, Lee DJ. Generalized characteristic boundary conditions for computational acoustics. *AIAA Journal* 2000; **38**:2040–2049.
6. Whitham GB. *Linear and Nonlinear Waves*. Wiley: New York, 1974.
7. Thompson KW. Time dependent boundary conditions for hyperbolic systems. *Journal of Computational Physics* 1987; **68**:1–24.
8. Bruneau CH, Creuse E. Towards a transparent boundary conditions for compressible Navier–Stokes equations. *International Journal for Numerical Methods in Fluids* 2001; **36**:807–840.
9. Prosser R, Schluter J. Toward improved boundary conditions for the DNS and LES of turbulents subsonic flows. *Technical Report*, Stanford University/NASA Ames, Center for Turbulence Research, *Proceeding of the CTR Summer Program*, 2004.
10. Moureau V, Lartigue G, Sommerer Y, Angelberger C. Numerical methods for unsteady compressible multi-component reacting flows on fixed and moving grids. *Journal of Computational Physics* 2005; **202**:710–736.
11. Baldwin B, Lomax H. Thin layer approximation and algebraic model for separated turbulent flows. *AIAA Paper 78-257*, 1978.
12. Jameson A. Time dependent calculations using multigrid with application to unsteady flows past airfoils and wings. *AIAA Paper 91-1596*, 1991.
13. Roe P. Approximate Riemann solvers, parameter vectors, and difference schemes. *Journal of Computational Physics* 1981; **43**:357–372.
14. Van Leer B. Towards the ultimate conservative difference scheme, III. *Journal of Computational Physics* 1977; **23**:263–275.
15. Rudy DH, Strikwerda JC. A nonreflecting outflow boundary condition for subsonic Navier–Stokes calculations. *Journal of Computational Physics* 1980; **36**:55–70.
16. Bogar TJ, Sajben M, Kroutil JC. Characteristic frequency and length scales in transonic diffuser flow oscillations. *AIAA Paper 81-1291*, 1981.
17. Hsieh T, Bogar TJ, Coakley TJ. Numerical simulation and comparison with experiment for self-excited oscillations in a diffuser flow. *AIAA Journal* 1987; **25**:936–943.

